Coupling between gap plasmon polariton and magnetic polariton in a metallic-dielectric multilayer structure

Junxue Chen,[1] Pei Wang,[1,*] Zhuomin M. Zhang,[2] Yonghua Lu,[1] and Hai Ming[1]

[1]*Department of Optics and Optical Engineering, Anhui Key Laboratory of Optoelectronic Science and Technology, University of Science and Technology of China, Hefei, Anhui 230026, People's Republic of China*

[2]*George W. Woodruff School of Mechanical Engineering, Georgia Institute of Technology, Atlanta, Georgia 30332, USA*

(Received 22 April 2011; revised manuscript received 11 June 2011; published 4 August 2011)

The excitation of plasmons in a metallic nanostructure represents a feasible and practical approach for manipulating the propagation and absorption of light at the subwavelength scale. Of particular interest is the coupling between plasmons, which can be used to facilitate the spectral tunability and tailor the optical response of the structure. In this paper, we study the coupling between two highly localized plasmonic modes: gap plasmon polariton mode and magnetic polariton mode, supported by a metallic-dielectric multilayer structure. The strong coupling gives rise to the formation of hybrid plasmon modes and large mode splitting. These hybrid modes result in unique spectral-directional absorption characteristics in the structure. The findings hold promise in applications such as photonic and energy conversion systems as well as the design of plasmonic nanodevices.

DOI: 10.1103/PhysRevE.84.026603 PACS number(s): 41.20.−q, 73.20.Mf, 42.79.Dj, 52.35.Mw

I. INTRODUCTION

The coupling and hybridization phenomena of plasmonic modes excited in metallic nanostructures offer exotic optical properties that cannot be easily achieved with natural materials. These phenomena have received considerable attention from both fundamental and practical points of view [1–5]. Numerous exotic characteristics have been demonstrated, such as the plasmonic analog of electromagnetically induced transparency (EIT) constructed by the coupled radiative-subradiant plasmon elements [6,7], the negative magnetic permeability provided by the coupled metallic strips [8], and the stereometamaterials constructed by the coupled split-ring resonators with twist angles [9]. Furthermore, the coupling between the localized plasmon mode and the surface plasmon polariton (SPP) mode propagating along the interface of a metal and a dielectric also provide remarkable optical properties. When a periodic metal strip array, supporting the localized plasmon mode, is placed close to the metal surface, the resonance properties of the metallic strips can be strongly modified due to the coupling with surface plasmon modes on the metal surface [10,11]. In addition, the metallic strips can interact with their own image created by the metal film to form a magnetic polariton (MP) mode, which mimics the magnetic resonance mode of a double-wire system and represents unique spectral and directional radiative properties [12]. Recently, the effect of the coupled MP modes on radiative properties of double-layer nonslit arrays has also been discussed [13].

The metal-dielectric-metal structure can support the propagation of the gap plasmon polariton (GPP) mode resulting from the coupling effect of surface waves [14–16], which can achieve the subwavelength confinement of light and have important applications in nanoscale optical circuits [15,17] and enhanced optical nonlinearity [18]. Based on the coupling effect of the GPP mode in the metallic-dielectric multilayer structure, highly localized bulk mode [16] and negative refraction [19] have been demonstrated recently. However, in the structured metallic-dielectric multilayer, the interplay between the GPP mode and other plasmon modes or the cavity mode is of great importance for future plasmon engineering and deserves further investigation.

In this work, a metallic grating coated on a dielectric spacer is introduced onto a metal-dielectric-metal (MDM) waveguide. In addition to the GPP mode, the structure can also support the MP mode. The excitation of the MP mode can strongly localize the electromagnetic energy into the dielectric layer underneath the metal strip. The localized near-field energy can be used to efficiently excite the GPP mode. More importantly, the anticrossing behavior with large mode splitting can be observed due to the strong coupling between MP and GPP modes. With regards to the reverse symmetry of field, the hybrid modes resulting from the coupling with even- and odd-order MP modes represent different excitation behaviors, which contribute to the remarkable spectral and directional absorption properties of the structure. Furthermore, the effect of geometric structure on the energy coupling between different modes is also examined.

II. DISPERSION RELATIONS

The proposed structure consists of a periodic metal strip array with a dielectric spacer deposited on top of an MDM waveguide, as illustrated in Fig. 1. The whole structure is assumed to be infinitely extended in the x direction. A TM-polarized (the magnetic field component is parallel to the y axis) electromagnetic wave is incident from air on the structure at an angle θ. In the present work, silver is selected as the material for the strips and cladding of the waveguide, and SiO_2 is used for the spacer and waveguide layer. The permittivity of SiO_2 is assumed to be constant and taken as 2.25. The frequency-dependent dielectric function of silver is taken from Ref. [20]. The rigorous coupled-wave analysis (RCWA) [21] was used to calculate the spectral response of the structure, and the absorption is 1 minus the reflectance, i.e., $\alpha = 1 - R$. In the calculation, the employed number of harmonics in the grating region was chosen to be 121, which

*Corresponding author: wangpei@ustc.edu.cn

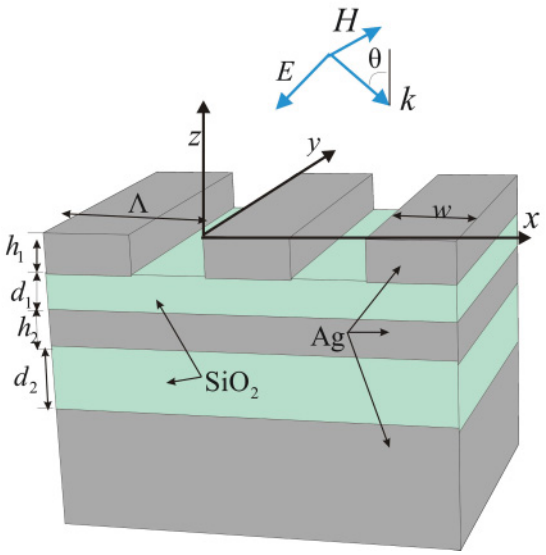

FIG. 1. (Color online) Schematic of the metamaterial nanostructure consisting of a periodic metallic strip array positioned atop a metal-dielectric-metal (MDM) waveguide, separated by a spacer layer with a thickness d_1. Here, Λ is the grating period; w and h_1 are the width and thickness of metal strips, respectively. The MDM waveguide is composed of a dielectric layer with a thickness d_2 sandwiched between two metal films. The thickness of the upper metal film is h_2. The bottom metal film is considered opaque with a thickness much greater than the penetration depth of light. A TM-polarized plane wave is incident on the structure at an angle θ.

is sufficient to provide the needed accuracy. Unless otherwise stated, the grating period is taken as $\Lambda = 400$ nm, the width of metal strip is set to $w = 300$ nm, the thickness of the spacer layer is $d_1 = 20$ nm, and the geometrical parameters of the MDM waveguide are $h_2 = 20$ nm and $d_2 = 50$ nm in the numerical simulation.

When the spacer layer is absent, the structure describes the typical interaction between a grating and a waveguide. The GPP mode can be excited by the periodic alignment of metal strips. The contour plot of the spectral-directional absorptance α in terms of photon energy and the parallel wave vector component K_x (divided by 2π) is shown in Fig. 2(a). Note that $K_x = (\omega/c)\sin(\theta)$. In Fig. 2, darker colors represent lower absorption, whereas bright colors correspond to higher absorption. The region outside the light line in the lower-right-hand corner is left blank. From Fig. 2(a), it is clear that absorption can be greatly enhanced when the GPP modes are excited. The excitation frequencies of GPP modes can be predicted with the grating equation:

$$\frac{\omega}{c}\sin(\theta) \pm m\frac{2\pi}{\Lambda} = \pm\beta(m = 1\cdots n), \qquad (1)$$

where m is the diffraction order of grating, and β is the magnitude of the wave vector associated with the GPP mode. According to the Bloch-Floquet condition, the dispersion of the GPP mode is folded into the region $K_x \leqslant \pi/\Lambda$. The branch labeled GPP(-1) at frequencies lower than 1.4 eV corresponds to the mode excited by the -1 diffraction order and the higher frequency branch labeled GPP(1) is associated with the $+1$ diffraction order. Similarly, SPP modes propagating along the

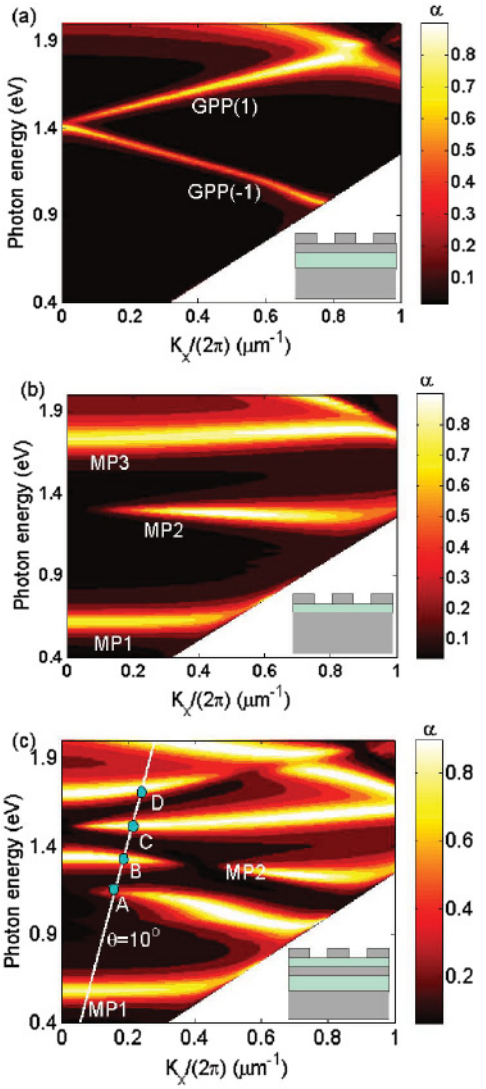

FIG. 2. (Color online) Contour plots of the spectral-directional absorptance: (a) the structure without spacer layer; (b) the structure without waveguide layer; (c) the composite structure shown in Fig. 1.

interface between the metal grating and air can also be excited. For the same diffraction order, the dispersion curve of SPP is located at higher frequencies and is not studied here.

The contour plot of absorptance is shown in Fig. 2(b) for the structure without a waveguide layer. It exhibits several absorption bands, which are attributed to the excitation of MP modes. The multiple magnetic polariton branches, denoted as MP1, MP2, and MP3, correspond to the fundamental, second, and third harmonic resonances, respectively. Their optical properties have been particularly studied in Ref. [12]. In contrast to the GPP mode, K_x has little effect on the absorption bands. The resonance frequency of the MP mode is mainly determined by the strip width w rather than the grating period or incidence angle.

Figure 2(c) shows the contour plot of absorptance for the composite structure shown in Fig. 1. The dispersion characteristics of both GPP and MP modes are exhibited. Compared with results shown in Fig. 2(a), much more intense light absorption and much wider absorption spectral

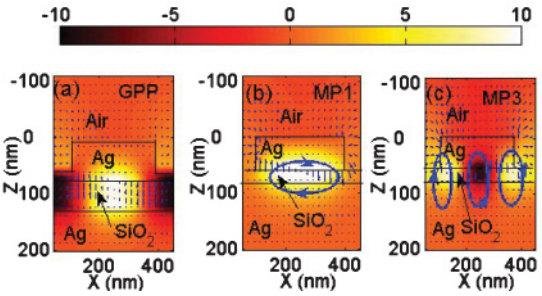

FIG. 3. (Color online) The spatial magnetic fields distribution for normal light incidence and TM polarization: (a) GPP, at 1.4 eV; (b) MP1, at 0.61 eV; (c) MP3, at 1.73 eV, which correspond to the spectral positions of absorption maxima shown in Figs. 2(a) and 2(b) at wave vector $K_x = 0$, respectively. The arrows represent electric field vectors, and the loops illustrate induced electric currents.

width are observed. This indicates the enhanced excitation efficiency of the GPP mode through introducing the spacer layer. More importantly, the dispersion curves of the GPP and MP modes are strongly modified, forming the multiple absorption branches in the spectrally overlapping regions. Here, we are interested in the four absorption branches labeled *A–D,* which are obtained from the intersections with the line $\theta = 10^\circ$. Clearly, branches *A* and *D* describe the dispersion similar to the GPP(−1) mode and MP3 mode, respectively, by comparison with Figs. 2(a)–2(c). It should be noted that branches *B* and *C* are the new energy branches that represent the unique dispersion property with weak angle dependence. Furthermore, a large band gap is also observed between branches *B, C,* and *D*, which is difficult to achieve using the grating-waveguide structure shown in Fig. 2(a).

Before discussing the interaction between the GPP mode and the MP mode, let us review their field structures. The magnetic field distributions are calculated with RCWA and displayed in Fig. 3 for normal incidence and TM polarization. The contour represents the amplitude of the magnetic field, and the arrows indicate the electric field vectors. The loops indicate induced electric current with arrows pointing in the electric field direction. Figure 3(a) shows the field distribution at 1.4 eV, corresponding to the spectrum position of the absorption maximum shown in Fig. 2(a) at wave vector $K_x = 0$. Due to the excitation of the GPP mode, there exists strong field confinement in the waveguide layer. Figures 3(b) and 3(c) show the field distributions at 0.61 and 1.73 eV, respectively, corresponding to the spectrum positions of absorption maxima shown in Fig. 2(b) at wave vector $K_x = 0$. Similar to the metallic strip pairs [8], the oscillating magnetic field parallel to grating grooves can cause antiparallel currents in the metal strips and the metal film surface. The antiparallel currents result in a diamagnetic response [12,22]. The diamagnetic response is then coupled with the metal film to cause strong field localization between the metal strips and the metal film. It is the field localization that is responsible for the strong light absorption in the spectrum. It is noted that one and three antinodes of magnetic field are formed in the spacer layer underneath the metal strip shown in Figs. 3(b) and 3(c), indicating, respectively, the excitation of MP1 and MP3. As illustrated in Fig. 2(b), MP2 can only be excited by inclined incidence due to the symmetry of field [12].

Furthermore, the periodic arrangement of metal strips provides the necessary momentum to couple the MP mode with the GPP mode for the composite structure shown in Fig. 1. For a given thickness d_2 of the MDM waveguide and incidence angle, the resonance frequency of the GPP mode is determined by the grating period Λ. The resonance frequency of the MP mode, however, is determined by the geometrical parameters of metallic strips and the thickness of the spacer layer for given materials [12,22]. Consequently, the resonance spectrum of the MP mode can overlap with that of the GPP mode through adjusting the structural parameters.

III. PHYSICAL MECHANISMS

In order to visualize the interaction between the GPP and MP modes of different order, the contour plot of absorptance as a function of frequency and strip width w is shown in Fig. 4(a) at $\theta = 10^\circ$. To facilitate the comparison, the contour plot of absorptance for the structure without a waveguide layer is shown in Fig. 4(b), where the two horizontal lines correspond to the resonance frequencies of GPP modes predicted from Eq. (1). The strong absorption shown in Fig. 4(b) is attributed to the excitation of the uncoupled MP modes, whose resonance frequencies decrease with increasing strip width. According to the theoretical prediction, when the width of the metal strip is taken as 110 or 140 nm, the spectral position of

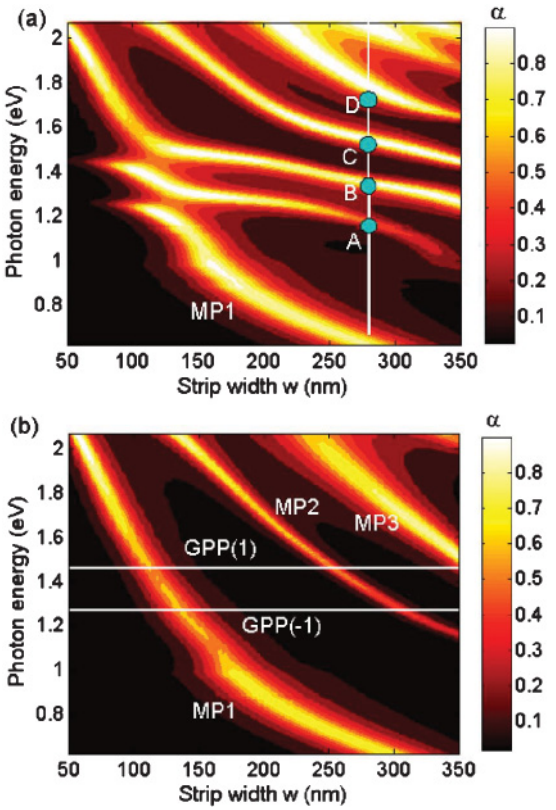

FIG. 4. (Color online) Contour plots of absorptance as a function of strip width w and frequency at incidence angle $\theta = 10^\circ$ for (a) the composite structure shown in Fig. 1; (b) the structure without the waveguide layer.

the MP1 mode will overlap with that of GPP(1) mode or GPP(−1) mode at frequency 1.46 or 1.27 eV, respectively. In this spectral region, the coupling between the two modes can be established. This is shown in Fig. 4(a) where the energy anticrossing behavior in the absorption spectrum can be clearly seen. Similarly, the spectral overlap between the MP2 mode and GPP mode is expected as the strip width is between 260 and 320 nm, according to the prediction. However, the energy anticrossing behavior does not appear in the absorption spectrum. Moreover, the interesting energy branches have four intersections with the vertical line at $w = 300$ nm as shown in Fig. 4(a). The four intersections are identical to those shown in Fig. 2(c) and are also labeled *A*–*D*. Comparing Fig. 2(c) with Fig. 4(a), branches *A*, *B*, and *C* exhibit the characteristics of both the GPP and MP modes. Their resonance frequencies decrease with increasing strip width and exhibit a weak angle dependence. Thus, we can deduce that branches *A*, *B*, and *C* originate from excitation of the hybrid modes of GPP and MP. The coupling with the MP mode gives rise to the new dispersion property. A detailed analysis of the coupling behavior between the MP mode and GPP mode will be given in subsequent sections.

The finite-difference frequency domain (FDFD) method is adopted through the use of an auxiliary field to accurately calculate the eigenmode supported by this periodic structure [23]. Here, the permittivity of silver is modeled with the Drude formula for free electron gas, $\varepsilon(\omega) = \varepsilon_\infty - \omega_p^2/\omega(\omega - i\Gamma_d)$, where ε_∞ describes the contribution to permittivity by the positive background of the ion cores [24], ω_p is the plasmon frequency of the free electron gas, and Γ_d is the scattering rate. The equation of motion of a free electron under an external electric field $\mathbf{E}$ is [24]

$$\frac{d^2\mathbf{r}}{dt^2} + \Gamma_d \frac{d\mathbf{r}}{dt} = \frac{e\mathbf{E}}{m}, \tag{2}$$

where m is the mass of the electron and e is the charge of the electron, which is negative. Note that electron scattering is modeled as a damping term with a damping coefficient Γ_d. Defining the polarization density $\mathbf{P} = Ne\mathbf{r}$, where N is the number density of electrons, we can express the equation of motion as follows:

$$\frac{d^2\mathbf{P}}{dt^2} + \Gamma_d \frac{d\mathbf{P}}{dt} = \varepsilon_0 \omega_p^2 \mathbf{E}, \tag{3}$$

where ε_0 is the permittivity of vacuum. Equation (3) is equivalent to the Drude model of metal whose plasma frequency is $\omega_p^2 = Ne^2/m\varepsilon_0$. The polarization current density is $\mathbf{J} = d\mathbf{P}/dt$. The basic equations of the electromagnetic field in a dispersive medium can be described as

$$\frac{\partial \mathbf{H}}{\partial t} = -\frac{1}{\mu_0}\nabla \times \mathbf{E}, \tag{4}$$

$$\frac{\partial \mathbf{E}}{\partial t} = \frac{1}{\varepsilon_0 \varepsilon_\infty}(\nabla \times \mathbf{H} - \mathbf{J}), \tag{5}$$

$$\frac{\partial \mathbf{J}}{\partial t} = \varepsilon_0 \omega_p^2 \mathbf{E} - \Gamma_d \mathbf{J}, \tag{6}$$

where μ_0 is the permeability of vacuum. Assuming that all fields vary as $\exp(i\omega t)$, we can obtain the eigenequation of the system as follows:

$$\begin{pmatrix} 0 & \frac{i}{\mu_0}\nabla\times & 0 \\ -\frac{i}{\varepsilon_0\varepsilon_\infty}\nabla\times & 0 & \frac{i}{\varepsilon_0\varepsilon_\infty} \\ 0 & -i\varepsilon_0\omega_p^2 & i\Gamma_d \end{pmatrix} \begin{pmatrix} \mathbf{H} \\ \mathbf{E} \\ \mathbf{J} \end{pmatrix} = \omega \begin{pmatrix} \mathbf{H} \\ \mathbf{E} \\ \mathbf{J} \end{pmatrix}. \tag{7}$$

It should be noted that all coefficients in Eq. (7) are frequency independent and the dispersive property of material is taken into account by introducing the auxiliary field [23]. For a specific geometry, Eq. (7) can be discretized with the finite difference method [25,26]. In the simulation, we set $\omega_p = 0$ and $\Gamma_d = 0$ for the air and dielectric regions. This ensures that the $\mathbf{J}$ field is not present in these regions. Then, the eigenmodes and optical band structure of system can be accurately calculated through solving the eigenequation with the FDFD method.

A. Coupling with the MP1 mode

For the coupling between the GPP and MP1 modes**,** Fig. 5(a) shows the contour plot of absorptance as a function of grating period Λ and frequency at normal incidence. As the grating period increases, the broad magnetic resonance absorption spectrum exhibits an anticrossing behavior with that of the GPP mode resonance. The anticrossing behavior can be explained in terms of the polariton model [27,28], which describes the coupling behavior of the original "bare" modes in the system. The effective Hamiltonian H_{eff} of the system near the center of the first Brillouin zone can be written as follows:

$$H_{\text{eff}} = \begin{pmatrix} E_{\text{GPP}} - i\gamma + \tilde{c}K_x & V_1 & V_2 \\ V_1 & E_{\text{GPP}} - i\gamma - \tilde{c}K_x & V_2 \\ V_2 & V_2 & E_{\text{MP}} - i\Gamma \end{pmatrix}, \tag{8}$$

where E_{GPP} and γ are the energy and the damping loss of the GPP mode, $\tilde{c}$ is the group velocity, $E_{\text{GPP}} - i\gamma \pm \tilde{c}K_x$ are the bare energies of GPP modes near momentum $K_\pm = \pm 2\pi/\Lambda$ [27], E_{MP} and $\Gamma$are the energy and the damping loss of the MP mode, V_1 is the energy coupling between the symmetric and asymmetric GPP mode, and V_2 is the coupling energy between the GPP and MP modes. The coupling behavior can be described by introducing V_1 and V_2 in Eq. (8). The eigenvalues of Eq. (8) represent the new eigenfrequencies of the coupled system. The corresponding eigenvectors of Eq. (8) represent the new hybrid modes. The amplitude of coupling parameters V_1 and V_2 can be estimated from the photonic band gap shown in Figs. 2(a) and 2(c). In Fig. 2(a), a minigap is formed at the wave vector $K_x = 0$, which results from the energy coupling between the symmetric and asymmetric GPP modes. However, the photonic band gap can be greatly enlarged due to the energy coupling between GPP and MP modes as shown in Fig. 2(c). It indicates that the coupling parameter V_1 is very small compared with the coupling parameter V_2. To simplify

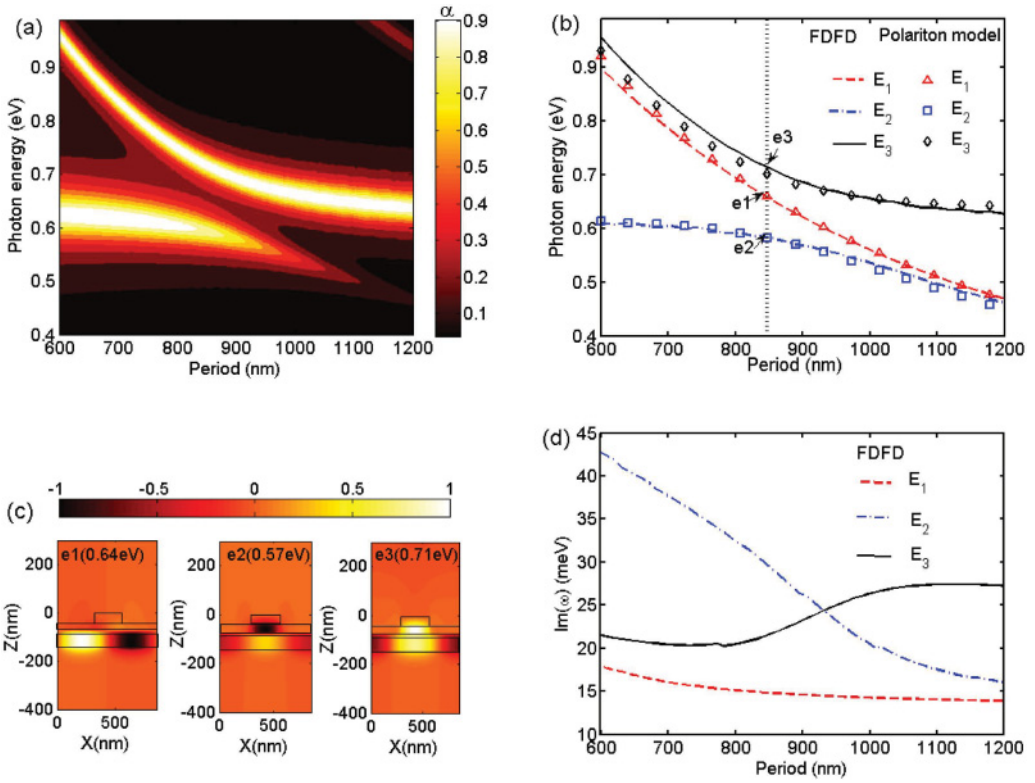

FIG. 5. (Color online) (a) Contour plot of absorptance as a function of grating period and frequency, showing the coupling between the GPP mode and MP1 mode at normal incidence; (b) the dependence of eigenfrequency of system on the grating period. The lines denote the results obtained from Eq. (7) with FDFD calculation and the symbols are obtained from the polariton model; (c) the normalized magnetic field distribution of eigenmodes with grating period 850 nm; (d) the imaginary part of the eigenfrequency of the system as a function of grating period. In the simulation, the parameters of the Drude model of silver are taken as $\varepsilon_\infty = 4.0$, $\omega_p = 1.33 \times 10^{16}$ rad/s, and $\gamma = 1.33 \times 10^{14}$ rad/s, respectively.

the discussion, a reasonable approximation is to neglect the coupling parameter V_1. In the case of normal incidence ($K_x = 0$), the three eigenvalues of the Hamiltonian can be expressed as

$$E_1 = E_{\mathrm{GPP}} - i\gamma, \tag{9}$$

$$E_{2,3} = 0.5\Big\{(E_{\mathrm{GPP}} + E_{\mathrm{MP}}) - i(\gamma + \Gamma) \pm\sqrt{[(E_{\mathrm{GPP}} - E_{\mathrm{MP}}) - i(\gamma - \Gamma)]^2 + 8V_2^2}\Big\}. \tag{10}$$

When the frequency of the GPP mode is equal to that of the MP mode, the mode splitting between the hybrid modes E_2 and E_3 is equal to $\sqrt{8V_2^2 - (\gamma - \Gamma)^2}$. Figure 5(b) illustrates the eigenfrequency of the system as a function of the grating period. The symbols represent the calculation from Eqs. (9) and (10), while the lines are the numerical solutions of Eq. (7) obtained from the FDFD method. Clearly, the two methods are in good agreement. Interestingly, branch E_1 is decoupled from the MP mode, whose eigenfunction $|\psi(E_1)\rangle = [|\psi_1\rangle, |\psi_2\rangle, |\psi_3\rangle]^T$ exhibits only the component of asymmetric GPP mode with $|\psi_1\rangle = -|\psi_2\rangle$ but no MP mode component since $|\psi_3\rangle = 0$ [28]. However, the eigenfunctions of branches E_2 and E_3 contain both GPP and MP components. To better understand the coupling mechanism, the normalized magnetic field distributions, obtained from Eq. (7), of the eigenmodes with grating period 850 nm and wave vector $K_x = 0$ are shown in Fig. 5(c). It can be seen that the magnetic field of mode e1 (located at 0.64 eV) is mostly localized in the waveguide layer with little energy emerging in the spacer layer. On the other hand, the magnetic fields of modes e2 (located at 0.57 eV) and e3 (located at 0.71 eV) exhibit not only the localized energy in the waveguide layer, but also a strong field localization in the spacer layer underneath the metal strip; suggesting that these two modes are coupled GPP and MP1 modes. From the field distributions, it can be deduced that mode e1 cannot be excited with normal incidence due to the antisymmetric field distribution. In contrast, modes e2 and e3 with symmetric field distributions can be strongly coupled with normally incident light, as demonstrated in Fig. 5(a). Furthermore, the loss for each eigenmode can also reflect the hybrid behavior between the GPP mode and MP mode. The imaginary part of eigenfrequency ω, corresponding to the loss of the mode, is shown in Fig. 5(d) as a function of the grating period. Due to the decoupling with the MP mode, the loss of branch E_1 is mostly from the absorption of metal, and it decreases gradually with increasing grating period and reaches a constant when $\Lambda > 900$ nm. In contrast, as the grating period is increased, the loss of branch E_2 or E_3 rapidly increases or decreases, respectively, due to the hybridization of modes.

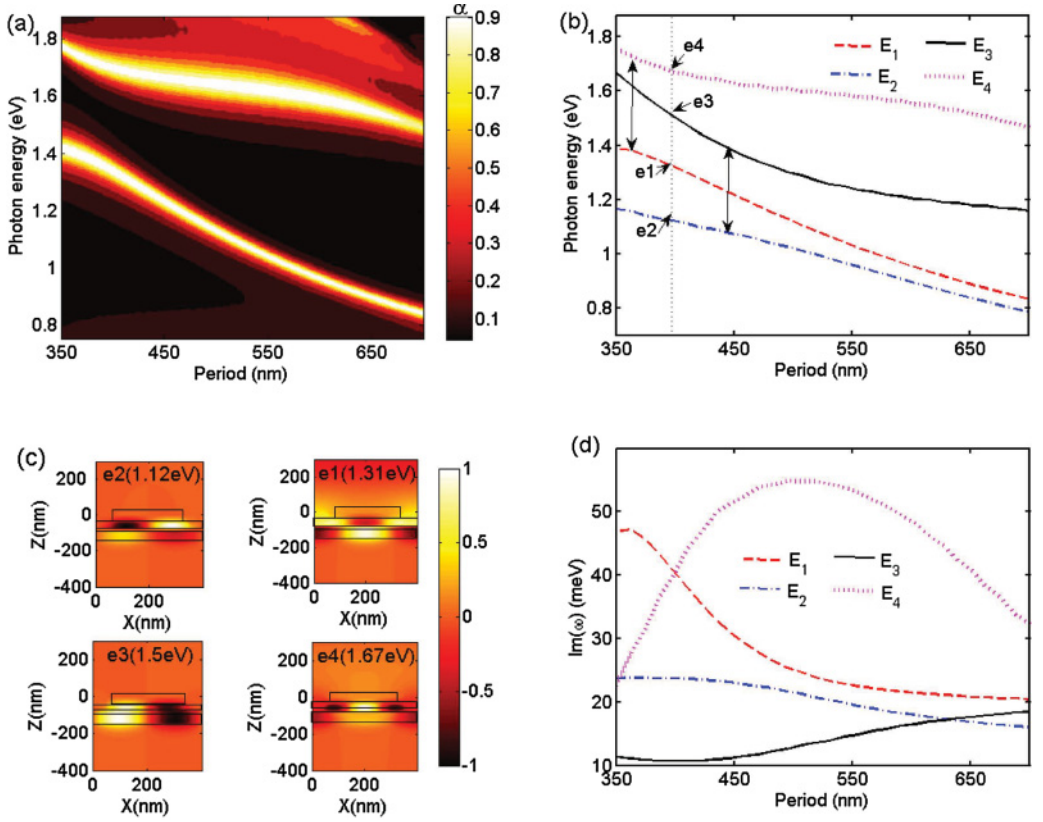

FIG. 6. (Color online) (a) Contour plot of absorptance as a function of grating period and frequency, showing the coupling between the GPP mode and higher-order MP modes at normal incidence; (b) the dependence of eigenfrequency, obtained from Eq. (7) with FDFD method, of the system on the grating period; (c) the normalized magnetic field distribution of eigenmodes with grating period 400 nm; (d) the imaginary part of the eigenfrequency of the system as a function of grating period.

B. Coupling with higher-order MP mode

The coupling behavior between the GPP mode and higher-order MP modes can also be analyzed using this method. Figure 6(a) shows the contour plots of absorptance as a function of grating period and frequency at photon energies from 0.8 to 1.9 eV. The corresponding eigenfrequencies of the system, obtained from Eq. (7) using the FDFD method, are shown in Fig. 6(b). Unlike the coupling with MP1 mode, the system represents the coupling among four modes and cannot be described using Eq. (8). In order to correspond to the case shown in Fig. 5(b), the branches are labeled E_1–E_4. While the energy anticrossing behavior also appears in the eigenfrequency diagram as in the case of coupling with MP1 mode, it does not appear in the absorption spectrum as shown in Fig. 6(a). To better understand this phenomenon, the normalized magnetic field distributions of the eigenmodes with grating period 400 nm and wave vector $K_x = 0$ are shown in Fig. 6(c). It can be seen that these modes exhibit strong energy localization in both the waveguide layer and spacer layer, suggesting that these modes are coupled GPP and MP modes. For modes e2 (located at 1.12 eV) and e3 (located at 1.5 eV), antisymmetric field distributions appear in the waveguide layer and spacer layer. The magnetic fields localized in the spacer layer exhibit two antinodes underneath the metal strip, indicating these two modes are coupled asymmetric GPP and MP2 modes. This is opposite to the case of the MP1 mode, which is the coupling with symmetric GPP mode. However, modes e1 (located at 1.29 eV) and e4 (located at 1.65 eV) exhibit the symmetric field distribution both in the waveguide layer and spacer layer. The magnetic fields localized in the spacer layer exhibit three antinodes underneath the metal strip, suggesting these two modes result from the coupling between symmetric GPP mode and MP3 mode. In view of the strong coupling between the GPP mode and MP mode, as well as the small separation in the resonance frequencies between the MP2 and MP3 modes, this system represents the coupling among four modes (two GPP modes, MP2 mode, and MP3 mode) and exhibits double mode splitting in the eigenfrequency diagram shown in Fig. 6(b).

The hybridization of modes can also be understood by analyzing the dependence of eigenmode loss on the grating period. As shown in Fig. 6(d), the loss of branch E_2 or E_3 is strongly changed around $\Lambda = 450$ nm due to the coupling with MP2 mode. Considering the higher resonance frequency of MP3 mode, the coupling with MP3 mode can be achieved by decreasing the grating period. Therefore, the loss of branch E_1 or E_4 exhibits rapid changes at smaller grating period as a result of coupling with MP3 mode. Furthermore, the loss of branch E_4 is also strongly changed around $\Lambda = 550$ nm. This is due to the coupling with other modes and is not studied here. Another characteristic is that the loss of branch E_1 or

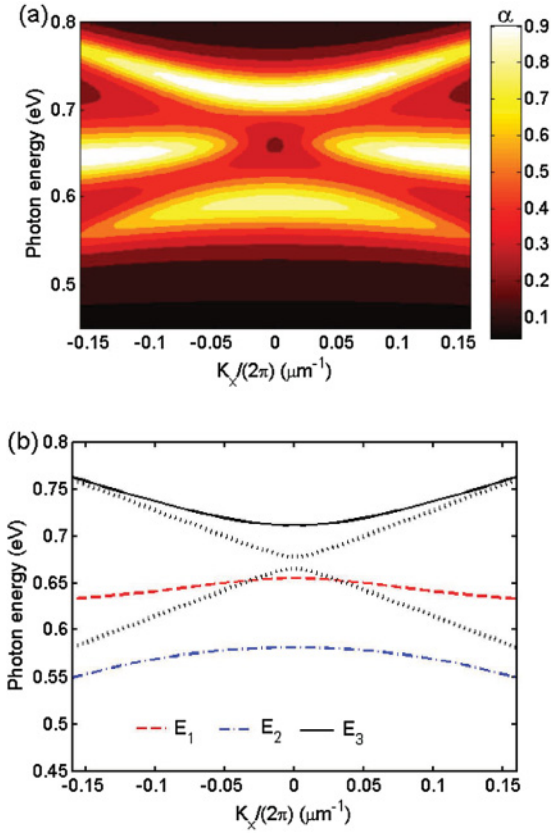

FIG. 7. (Color online) The dispersion characteristics of the coupled modes between GPP mode and MP1 mode: (a) contour plot of absorptance as a function of wave vector K_x and frequency with grating period 850 nm; (b) the corresponding eigenfrequency of the system versus the wave vector K_x. In the absence of the spacer layer, the eigenfrequency of grating-induced GPP mode are also shown with dotted lines.

E_4 is larger than that of branch E_2 or E_3 due to a large radiative damping. Hence, when light is incident normally on the structure, only branches E_1 and E_4 can be excited with regards to the symmetry of the field. This explains why there are only two branches in the absorption spectrum shown in Fig. 6(a).

C. Angle dependence of the hybrid modes

We now examine the angle dependence of hybrid modes. Figure 7(a) shows the contour plot of absorptance as a function of wave vector K_x and frequency for the structure with grating period 850 nm. It is noted that two absorption peaks appear at normal incidence and a clear splitting into three absorption peaks is observed at the inclined incidence due to the decoupling with MP1 mode. The eigenfrequency of system as a function of wave vector K_x is shown in Fig. 7(b). When the spacer layer is absent, the eigenfrequency (denoted by dotted lines) describes the dispersion of grating-induced GPP mode. The GPP mode is folded into the Brillouin zone. The degeneracy of the mode is lifted at the center of the zone ($K_x = 0$) and a small band gap appears due to the reverse symmetry of fields at the band edge. For the structure with the spacer layer, the eigenfrequency (labeled E_1–E_3) of the primary degenerate mode is further lifted at the zone center

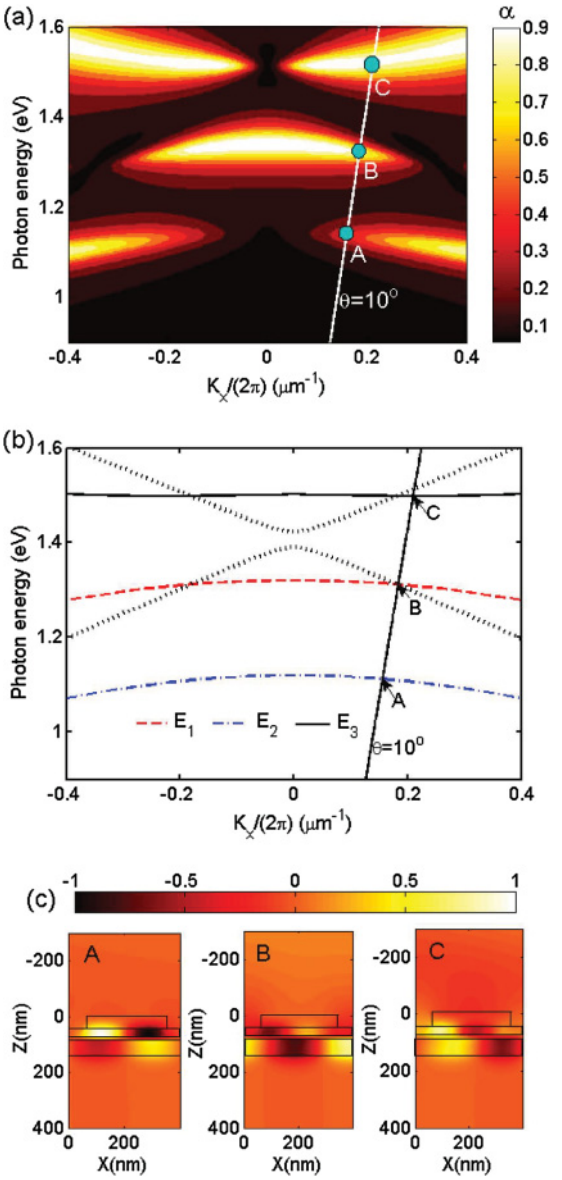

FIG. 8. (Color online) The dispersion characteristics of the coupled modes between GPP mode and higher-order MP mode: (a) contour plot of absorptance as a function of wave vector K_x and frequency with grating period 400 nm; (b) the corresponding eigenfrequency of the system as a function of wave vector K_x. Similarly, the dotted lines denote the eigenfrequency for the structure without spacer layer; (c) the normalized magnetic field distributions of eigenmodes corresponding to the intersections with line $\theta = 10^\circ$.

as a result of the coupling with MP1 mode. A large band gap is formed and contributes to the lower absorption as shown in Fig. 7(a).

When the grating period is set to 400 nm, the contour plot of absorptance as a function of wave vector K_x and frequency is shown in Fig. 8(a). There is only one absorption peak at normal incidence and the other two absorption peaks appear at inclined incidence. The corresponding eigenfrequency of the structure is illustrated in Fig. 8(b). Similar to the case of coupling with MP1 mode, the coupling with MP2 mode also enlarges the mode splitting of the grating-induced GPP mode

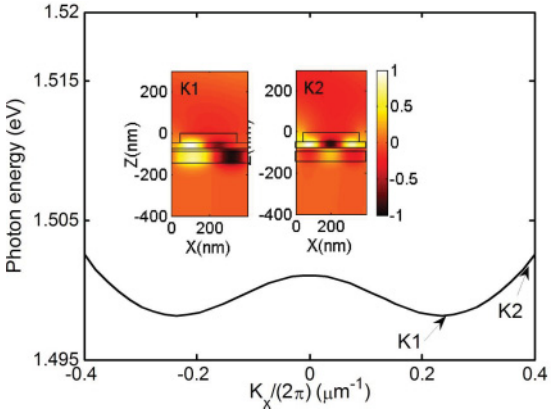

FIG. 9. (Color online) The magnified plot of energy branch E_3 shown in Fig. 8(b), where the normalized magnetic field distributions corresponding to the points $K1$ and $K2$ are shown in the inset.

(denoted by dotted lines). Furthermore, the energy branches have three intersections with the line $\theta = 10^\circ$ as shown in Figs. 8(a) and 8(b). Like the case shown in Fig. 2(c), the three intersections are labeled A–C. The normalized magnetic field distributions of eigenmodes, obtained from Eq. (7), corresponding to these intersections are shown in Fig. 8(c), which exhibit similar distributions as the modes e1, e2, and e3 shown in Fig. 6(c). Here, the symmetry of field is changed due to the wave vector $K_x > 0$. Branches A and C can be excited by inclined incidence. Hence, the claim in Sec. III that branches A, B, and C are the hybrid modes of GPP and MP is reasonable.

More importantly, the dispersion of branch E_3 exhibits a weak angle dependence in contrast to that of the bare GPP mode. The magnified plot of the eigenfrequency of branch E_3 as a function of wave vector K_x is shown in Fig. 9. It is noted that the eigenfrequency of branch E_3 is again not increased or decreased progressively but exhibits much more complicated behavior. The magnetic field distributions of the two particular points (labeled $K1$ and $K2$) corresponding to the frequency minimum and maximum in the range of calculations are shown in the inset. For the field distribution at point $K1$, the mode is still considered as the hybrid of GPP mode and MP2 mode from the previous analysis, but the mode is changed into the bare MP3 mode at the point $K2$. Because the eigenfrequency of GPP(1) mode is increased with increasing K_x, branch E_3 is mostly from the hybrid between GPP(1) mode and MP2 mode at small wave vector. When the wave vector K_x is further increased, the GPP(1) mode decouples with MP2 mode due to the increased eigenfrequency, but couples with MP3 mode. This coupling still leads to the energy anticrossing behavior which can be observed between energy branches C and D shown in Fig. 2(c). Therefore, the resonance frequency of MP3 mode is greatly modified due to the coupling with GPP(1) mode and the dispersion of the MP3 mode is divided into two branches C and D. This is the reason why the dispersion of energy branch C shown in Fig. 2(c) exhibits weak angle dependence.

D. Geometric effects on energy coupling

The dependence of the coupling energy between the GPP mode and MP mode on the geometric parameters of the structure is also studied. Here, we only focus on the coupling

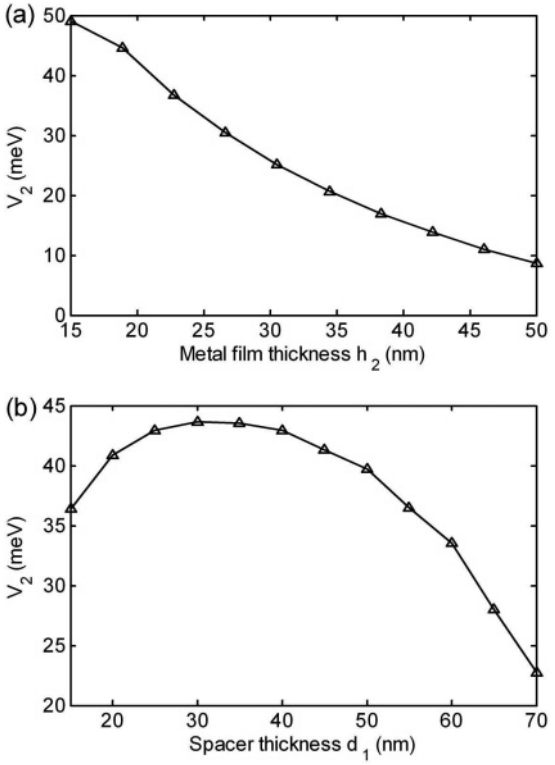

FIG. 10. (a) The coupling energy V_2 as a function of the metal film thickness h_2 with grating period 850 nm and the spacer thickness 20 nm; (b) the coupling energy V_2 as a function of the spacer thickness d_1 with metal film thickness $h_2 = 20$ nm.

with MP1 mode since it can be well described using the polariton model of three modes. By fitting the eigenfrequency expressed in Eq. (10) to the results obtained from Eq. (7), the coupling parameter V_2 can be extracted. The dependence of the coupling parameter V_2 on the metal film thickness h_2 is shown in Fig. 10(a). The electromagnetic field is exponentially attenuated in the metal film due to the negative permittivity of metal. The evanescent field that can penetrate through the metal cladding decreases with increasing h_2; this results in a reduction of the interaction intensity between the GPP mode and MP mode and leads to the smaller coupling energy V_2 as illustrated in Fig. 10(a). The thickness d_1 of the spacer layer is also an important parameter that can affect the resonance frequency and energy localization of the MP mode. Figure 10(b) shows the coupling parameter V_2 as a function of d_1. It is noted that there exists an optimal spacer thickness to generate the maximum coupling intensity between the GPP mode and MP mode. As the spacer thickness increases, the interaction zone of the GPP mode and MP mode is enlarged. On the other hand, the field localization of MP mode is decreased [29], causing a reduction in the interaction intensity between modes. These two factors together determine the coupling behavior between the GPP mode and MP mode and lead to the optimal spacer thickness.

IV. CONCLUSION

In summary, this study elucidates the coupling behavior between the GPP mode and MP mode in a metallic-dielectric multilayer structure. The large mode splitting is observed as

a result of the strong mode coupling. Furthermore, due to the opposite field symmetry, the odd- and even-order MP modes exhibit different mode selections during the coupling with GPP mode. These hybrid modes exhibit different excitation behaviors at normal incidence; this leads to the remarkable spectral-directional absorption property of the structure. The studied phenomena may find applications in photonic and energy conversion systems, plasmon engineering, and the design of alternative metamaterials.

ACKNOWLEDGMENTS

This work is supported by the National Key Basic Research Program of China (Grant No. 2011CB301802), the Key Program of the National Natural Science Foundation of China (Grant No. 61036005), and the National Natural Science Foundation of China (Grants No. 60977019, No. 11074240, No. 11074241). Z.M.Z. acknowledges the support from the US National Science Foundation (NSF CEBT No. 0828701).

[1] F. Lopez-Tejeira, S. G. Rodrigo, L. Martin-Moreno, F. J. Garcia-Vidal, E. Devaux, T. W. Ebbesen, J. R. Krenn, I. P. Radko, S. I. Bozhevolnyi, M. U. Gonzalez, J. C. Weeber, and A. Dereux, Nat. Phys. **3**, 324 (2007).

[2] F. J. Garcia-Vidal, S. G. Rodrigo, L. Martin-Moreno, F. J. Garcia-Vidal, E. Devaux, J. Dintinger, T. W. Ebbesen, J. R. Krenn, I. Radko, and S. I. Bozhevolnyi, New. J. Phys. **10**, 033035 (2008).

[3] F. Lopez-Tejeira, F. J. Garcia-Vidal, and L. Martin-Moreno, Phys. Rev. B **72**, 161405(R) (2005).

[4] E. Prodan, C. Radloff, N. J. Halas, and P. Nordlander, Science **302**, 419 (2003).

[5] J. A. Fan, C. H. Wu, K. Bao, J. M. Bao, R. Bardhan, N. J. Halas, V. N. Manoharan, P. Nordlander, G. Shvets, and F. Capasso, Science **328**, 1135 (2010).

[6] S. Zhang, D. A. Genov, Y. Wang, M. Liu, and X. Zhang, Phys. Rev. Lett. **101**, 047401 (2008).

[7] N. Liu, L. Langguth, T. Weiss, J. Kastel, M. Fleischhauer, T. Pfau, and H. Giessen, Nat. Mater. **8**, 758 (2009).

[8] V. M. Shalaev, W. S. Cai, U. K. Chettiar, H. K. Yuan, A. K. Sarychev, V. P. Drachev, and A. V. Kildishev, Opt. Lett. **30**, 3356 (2005).

[9] N. Liu, H. Liu, S. N. Zhu, and H. Giessen, Nat. Photonics **3**, 157 (2009).

[10] A. Christ, T. Zentgraf, S. G. Tikhodeev, N. A. Gippius, J. Kuhl, and H. Giessen, Phys. Rev. B **74**, 155435 (2006).

[11] A. Christ, G. Leveque, O. J. F. Martin, T. Zentgraf, J. Kuhl, C. Bauer, H. Giessen, and S. G. Tikhodeev, J. Microsc. (Oxford, UK) **229**, 344 (2008).

[12] B. J. Lee, L. P. Wang, and Z. M. Zhang, Opt. Express **16**, 11328 (2008).

[13] L. P. Wang and Z. M. Zhang, J. Opt. Soc. Am. B **27**, 2595 (2010).

[14] K. Park, B. J. Lee, C. Fu, and Z. M. Zhang, J. Opt. Soc. Am. B **22**, 1016 (2005).

[15] K. Tanaka and M. Tanaka, Appl. Phys. Lett. **82**, 1158 (2003).

[16] I. Avrutsky, I. Salakhutdinov, J. Elser, and V. Podolskiy, Phys. Rev. B **75**, 241402(R) (2007).

[17] G. Veronis, Z. F. Yu, S. E. Kocabas, D. A. B. Miller, M. L. Brongersma, and S. H. Fang, Chin. Opt. Lett. **7**, 302 (2009).

[18] J. X. Chen, P. Wang, X. L. Wang, Y. H. Lu, R. S. Zheng, H. Ming, and Q. W. Zhan, Appl. Phys. Lett. **94**, 081117 (2009).

[19] X. Fan, G. P. Wang, J. C. W. Lee, and C. T. Chan, Phys. Rev. Lett. **97**, 073901 (2006).

[20] *Handbook of Optical Constants of Solids*, edited by E. D. Palik (Academic, San Diego, 1998).

[21] B. J. Lee, Y. B. Chen, and Z. M. Zhang, J. Comput. Theor. Nanosci. **5**, 201 (2008).

[22] J. F. Zhou, E. N. Economon, T. Koschny, and C. M. Soukoulis, Opt. Lett. **31**, 3620 (2006).

[23] A. Raman and S. H. Fan, Phys. Rev. Lett. **104**, 087401 (2010).

[24] S. A. Maier, *Plasmonics: Fundamentals and Applications* (Springer, New York, 2007).

[25] C. Yu and H. Chang, Opt. Express **12**, 1397 (2004).

[26] C. Yu and H. Chang, Opt. Express **12**, 6165 (2004).

[27] A. Christ, S. G. Tikhodeev, N. A. Gippius, J. Kuhl, and H. Giessen, Phys. Rev. Lett. **91**, 183901 (2003).

[28] T. Zentgraf, S. Zhang, R. F. Oulton, and X. Zhang, Phys. Rev. B **80**, 195415 (2009).

[29] Y. Todorov, L. Tosetto, J. Teissier, A. M. Andrews, P. Klang, R. Colombelli, I. Sagnes, G. Strasser, and C. Sirtori, Opt. Express **18**, 13886 (2010).